ACS APPLIED MATERIALS & INTERFACES

Research Article

www.acsami.org

Characteristics of In-Substituted CZTS Thin Film and Bifacial Solar Cell

Jie Ge,*[,†,‡,§] Junhao Chu,*[,†,‡] Jinchun Jiang,[‡] Yanfa Yan,[§] and Pingxiong Yang[†]

[†]Key Laboratory of Polar Materials and Devices (Ministry of Education), East China Normal University, Shanghai 200241, China

[‡]Shanghai Center for Photovoltaics (SCPV), Shanghai 200081, China

[§]Wright Center for Photovoltaics Innovation and Commercialization, Department of Physics and Astronomy, The University of Toledo, Toledo, Ohio 43606, United States

Supporting Information

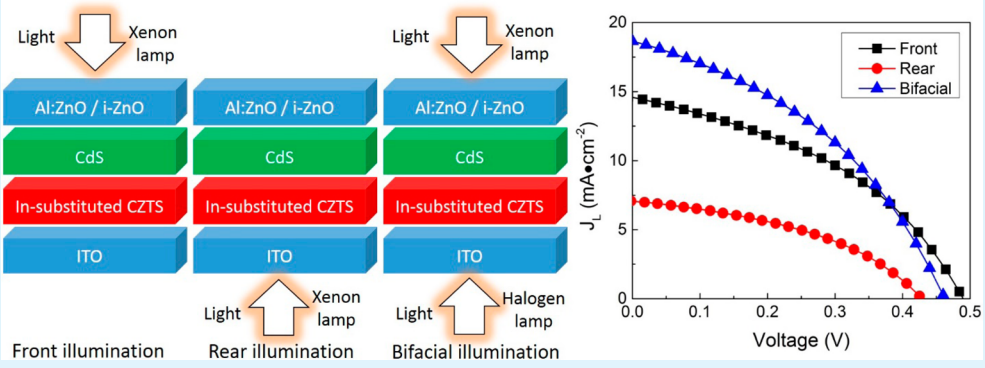

ABSTRACT: Implementing bifacial photovoltaic devices based on transparent conducting oxides (TCO) as the front and back contacts is highly appealing to improve the efficiency of kesterite solar cells. The p-type In substituted Cu_2ZnSnS_4 (CZTIS) thin-film solar cell absorber has been fabricated on ITO glass by sulfurizing coelectroplated Cu−Zn−Sn−S precursors in H_2S (5 vol %) atmosphere at 520 °C for 30 min. Experimental proof, including X-ray diffraction, Raman spectroscopy, UV−vis−NIR transmission/reflection spectra, PL spectra, and electron microscopies, is presented for the interfacial reaction between the ITO back contact and CZTS absorber. This aggressive reaction due to thermal processing contributes to substitutional diffusion of In into CZTS, formation of secondary phases and electrically conductive degradation of ITO back contact. The structural, lattice vibrational, optical absorption, and defective properties of the CZTIS alloy absorber layer have been analyzed and discussed. The new dopant In is desirably capable of improving the open circuit voltage deficit of kesterite device. However, the nonohmic back contact in the bifacial device negatively limits the open circuit voltage and fill factor, evidencing by illumination-/temperature-dependent $J-V$ and frequency-dependent capacitance−voltage ($C-V-f$) measurements. A 3.4% efficient solar cell is demonstrated under simultaneously bifacial illumination from both sides of TCO front and back contacts.

KEYWORDS: *bifacial thin-film solar cell, interfacial reaction, indium substituted CZTS, H_2S sulfurization, back contact*

INTRODUCTION

Kesterite thin films based on sulfide Cu_2ZnSnS_4 (CZTS), its selenide derivative $Cu_2ZnSnSe_4$ (CZTSe), and sulfur−selenium alloy $Cu_2ZnSn(S_x, Se_{1-x})_4$ (CZTSSe) are promising absorber materials for sustainable photovoltaics, because of the abundance, environmental benignity, and industrial compatibility of the constituent elements. To date, more than 12, 9, and 9% efficiencies have been achieved based on sulfur−selenium alloy CZTSSe,[1,2] pure CZTS,[3] and selenide CZTSe,[4] respectively. However, the device efficiency is limited by the dominant issue of high open circuit voltage (V_{OC}) deficits. The constituent element of multivalent Sn (i.e., II and IV oxidation states) is proved to create deep levels and thus limit the device efficiency.[5] Partial substitution of Sn by Ge could positively reduce the deep levels, increase minority carrier lifetime and improve the device efficiency due to its lower propensity toward the II oxidation state. To date, greater than 9% efficiency has been reported based on Ge-substituted CZTSSe absorbers.[6,7] The Ge-substituted CZTSSe should have bigger band gaps because of the upshift of conduction band. This shift in band gap contributes to an increase in V_{OC} of the device and loss in short circuit current (J_{SC}); however, the Ge substituted cell still suffers from the high V_{OC} deficit (673 mV).[6] Promisingly, D. B. Mitzi et al. successfully improved the V_{OC} deficit (593 mV) based on a bilayered emitter structure of In_2S_3/CdS/CZTSSe. After rapid postannealing, a great concentration of indium coming from the In_2S_3 emitter diffusion into CZTSSe layer consequently increased the carrier densities and improved the V_{OC} for given band gap via the

Received: September 3, 2014
Accepted: October 23, 2014
Published: October 23, 2014

formation of In_{Sn}^{-} shallow defects.[8] Actually, the electrical transport properties of indium substituted CZTSe alloy have been studied already.[9−11] The substitution of tin with indium can cause the significant increase in the conductivity, hole density, and mobility, which in turn merit the improvement of V_{OC} deficit. Thus, the new dopant of element indium (III group) could be probably attractive in the future.

Notably, the current research on kesterite is almost based on the typical substrate-type structured device with Mo back contact and transparent conducting oxide (TCO) front contact. There has seldom been reported the bifacial kesterite solar device, using TCO layers as both front and back contact. The bifacial device structure allows the sunlight incident from both front and rear contact, meriting the increased conversion efficiency. Besides, the bifacial device can be also potentially applied into the tandem devices, solar windows, solar house roof, etc. due to the transparent back contact allowing the sunlight pass through the entire solar cell. In practice, the bifacial device structure has been widely applied into the high efficient CIGS and Si based solar devices,[12−14] which creates a bright future for the development of bifacial kesterite solar device.

In this work, a cathodic coelectroplating technique was applied to fabricate Cu−Zn−Sn-S thin film precursors on ITO coated glass substrates. Via the sulfurization in the diluted H_2S atmosphere, an interfacial reaction between the ITO back contact and absorber layer, forming In substituted CZTS absorber, is presented. A 3.4% efficient solar device under bifacial illumination is achieved. The structural, lattice vibrational, optical absorption, and defective properties of the new CZTIS alloy have been investigated.

EXPERIMENTAL SECTION

Preparation. The cathodic coelectroplated Cu−Zn−Sn−S precursor films were prepared on ITO-coated glass substrates (~2.5 × 3 cm^2). A conventional three-electrode assembly with an Ag/AgCl (3 M KCl) reference, an inert Pt anode, and a working electrode ITO glass (NSG, 8 Ω/□, 150 nm). The precursor layer was deposited at −1.15 V versus Ag/AgCl in potentiostatic mode for 30 min at room temperature without stirring. The electrolyte, with a pH value of approximately 6.1, was consisted of sodium-citrate (100 mM) together with potassium tartrate (5 mM) as complexing reagents, metal sulfates of Cu (II) (10 mM), Zn (II) (50 mM), Sn (II) (10 mM) ions, sodium-thiosulfate (5 mM) and deionized water (200 mL). The composition of the precursor film (Zn/Sn = 1.0, Cu/Zn = 1.8, S/metals = 0.2) was Cu poor and Zn, Sn slightly rich. The sulfurization was carried out in a mixture gas of argon and H_2S (vol. 5%) ramping at 20 °C min^{-1} and dwelling at 520 °C for 30 min. In addition, the growth pressure during the sulfurization process was maintained at around 10 Torr. The sulfurized absorber film was immediately dipped in an alkaline bath for the deposition of an n-type CdS layer (approximately 80 nm). The growth of CdS layer uses chemical solutions of $CdSO_4$ (1.5 mM), thiourea (75 mM), and ammonium hydroxide (1.8 M) at 85 °C. Window layers of i-ZnO/ZnO:Al were sputtered through an aperture mask with an area of 0.07/0.09 cm^2. No metal grid and antireflection coating was deposited on the single cell; for the photo of the actual device, please see Figure S1 in the Supporting Information.

Characterization. Scanning electron microscope (SEM) analysis was conducted using Phillips S360 FE-SEM at a tilted angle of 10 degree on the sample films, which were cleaved prior to the SEM analyses and coated with a thin Au film to prevent charging effects. Samples for transmission electron microscope (TEM) analysis were prepared using the FEI Helios 400S DB−FIB and was attached to Mo grid. TEM images were taken using a FEI TECNAI G2 S-TWIN F20 TEM operated at 200 kV. The incident electron probe comprised 200 keV electrons in an incident probe of 0.7 nm full-width at half-maximum (fwhm). The selective area electron diffraction (SEAD) image of the absorber film was obtained with a selective area aperture of approximately 200 nm in diameter. Compositional results were acquired by energy-dispersive X-ray spectroscopy (EDX) equipped with FE-SEM using the standardless ZAF (atomic number, absorption and fluorescence) correction method for the precursor and with TEM for solar absorber films. Powder X-ray diffraction (XRD) data were collected using a Rigaku 69 D/max 2550 V diffractometer with Cu Kα lines (0.15418 nm) in $\theta-2\theta$ scans operated at 40 kV and 250 mA. A graphite monochromator and a large beam current (250 mA) of X-ray tube were used in order to reduce the measuring noises and collect the intense and deep enough crystalline information on the samples. Theta calibration was done using a standard Si sample prior to the XRD measurement. Raman spectroscopy (room temperature) was carried out using Nanofinder 30 (TII Tokyo Instruments) with a resolution of less than 1 cm^{-1} under parallel configuration. A polarized 532 nm beam excited by a solid state laser with a laser excitation power of 2 mW nearly normally stroke the sample surface. Raman shift was calibrated by the single crystal Si at 520.4 cm^{-1}. The transmission (T) and reflectance (R) of the absorber layer and ITO layer were performed using a Cary 5000 UV−vis−NIR spectrophotometer, where the transmission of the soda lime glass substrate was subtracted in terms of the baseline. The photoluminescence (PL) studies of the absorber layer were performed with a 532 nm solid-state laser. PL emission signals were collected using a liquid nitrogen cooled Ge detector.

Current−voltage characteristics of the bifacial device for one-side illumination (front and rear) were measured under AM 1.5 global spectrum with the irradiance set to 1000 W m^{-2} (1 sun; Xe lamp). The bifacial current−voltage characteristics were measured under the simultaneous illumination of Xe lamp (1 sun) from the front side of ZnO window layer and halogen lamp (~1 sun) from the rear side of ITO back contact (Figure S1 in the Supporting Information). External quantum efficiency (EQE) measurements were performed by a single source illumination system (halogen lamp) combined with a monochromator. As noted, the light beam of the EQE system with a size of 3 × 3 cm^2 is bigger than the cell area (0.07 cm^2), leading to underestimating the photogenerated currents of the bifacial device. A calibrated Si-cell was used as reference for the $J-V$ as well as for the EQE measurements. The frequency-dependent capacitance−voltage ($C-V-f$) measurements were performed at room temperature with a DC bias scanning from −0.8 to 0.8 V using the Dielectric Spectrometer BDS40, and 50 mV rms was used as the testing AC signal with selected frequencies.

RESULTS AND DISCUSSION

Figure 1 shows a SEM cross-section of a portion of the electrodeposited Cu−Zn−Sn−S precursor on ITO substrate. Uniform surface and compact cross-section extending through the thickness of the precursor film are visible. The cross-sectional SEM and bright field TEM images of the resulting device (Figure 1b, c) show a bilayered crystalline characteristic in the absorber layer. The upper layer of the absorber with a thickness of about 560 nm shows a large average grain size. The well-defined grain in the upper layer shown in the SEM image has a diameter of above 4 μm, which is consistent with the CZTS grains grown by H_2S.[15] However, the underlying layer (~500 nm) comprises of numerous small particulates. Notably, the boundary of ITO back contact and the absorber bottom layer has disappeared as seen from the device cross-sectional SEM or TEM images, in striking contrast with the precursor cross-section (Figure 1a), predicting an interfacial reaction between ITO back contact and absorber layer took place during the sulfurization process. This detrimental reaction has negatively contributed to the out-diffusion of In, a problematic underlying layer of the absorber, and the reduced conductivity of ITO back contact as shown below. It is partially related to the chemically active reducibility of H_2S gas.[16] Moreover, this interfacial reaction relies more on the sulfurization temperature. At T > 520 °C, as shown in Figure S2

in the Supporting Information, ITO substrate will completely react with the absorber and consequently result in the exhaustive loss of back contact for the solar device.

EDX equipped with TEM point analysis results of nine different positions across the absorber layer is shown in Table 1.

Table 1. EDS Elements Analysis by TEM for the Positions Denoted in Figure 1c

position	Cu (%)	Zn (%)	Sn (%)	In (%)	S (%)	O (%)
1	2.5	0.57	4.1	28.6	6.2	58.1
2	15.4	11.6	12.0	8.4	31.4	21.2
3	32.6	1.1	18.3	2.0	46.0	
4	46.8	1.6	14.3	1.1	36.2	
5	30.9	15.2	6.5	5.6	41.9	
6	27.9	16.2	5.9	7.3	42.6	
7	20.5	18.9	1.5	13.1	46.0	
8	25.9	15.3	3.5	10.6	44.7	
9	30.6	15.0	7.4	6.7	40.3	

During the EDX analysis, the stray electrons will hit the Mo grid holder and excite an intense EDX signal from Mo. Because of the overlap of L lines of Mo and the K lines of S in EDX, the S content shown in Table 1 is not ably representive of the true values. Furthermore, the upper layer grains shows a heavily Sn poor composition of Cu/Zn ∼ 2.04 (Position 5) and 2.03 (Position 9), as well as Zn/Sn ∼ 2.34 (Position 5) and 2.03 (Position 9). Else, EDX analysis also reveals the presence of In in the upper layer with the Sn/In ratios of 1.16 (Position 5) and 1.10 (Position 9, Figure 1f), demonstrating the out-diffusion of In from the ITO back contact into the CZTS absorber during the sulfurization. Sn and In are adjacent in the element periodic table and have the smallest mismatch in atomic size. Thus, In_{Sn}^{-} antisite acceptor should have the lowest formation energy, and the ion exchanges between In and Sn atoms should be the easiest. Otherwise, the lattice structure should be destructively instable because of the severe deficiency of Sn in the upper absorber layer. Further analyses are performed using high-resolution TEM (HRTEM) micrograph (Figure 1d) and selected area electron diffraction (SAED) (Figure 1e) images at Position 9 in the well-defined upper layer. The SAED and HRTEM images demonstrate the In substituted CZTS (CZTIS) upper layer is highly crystalline single crystal with a tetragonal structure. The interplanar spacing measured by Gatan software DigitalMocrograph (TM) 3.9.1 and the calculated lattice parameters are given in Table 2. As seen, the In substituted CZTS upper layer displays a largely expanded lattice compared to Cu_2ZnSnS_4 (PDF 97−018−9286). Such a large lattice expansion should correlate with In_{Sn}^{-} because of the bigger atomic/ionic radius of In 1.63/0.8(+III) Å than Sn 1.41/0.45(+IV) Å.[9] To remain charging neutrality, In_{Sn}^{-}will trigger the formation of a number of sulfur vacancies V_S^{2+} in the alloy. This provides a route to calculate the content of sulfur using the metallic percentages in Table 1, reliably. For Position 9, the chemical formula should be $Cu_{2.040}Zn_{1.000}(Sn_{0.493},In_{0.447})S_{3.677}$. The CZTIS alloy is, in fairness, highly compensated because of a great number of $2In_{Sn}^{-} + V_S^{2+}$ complex clusters. In addition, we note that occupational vacancies still exists at tin position, seeing that the total ratio ∼0.940 of Sn (0.493) and In (0.447) is smaller than 1. These vacancies may probably be occupied by copper or zinc, or just unoccupied, implying the likely presence of Cu_{Sn}^{3-}, Zn_{Sn}^{2-}, or V_{Sn}^{4-} acceptors.

In the particulate-like underlying layer, a set of problematic issues like phase segregation, nonuniformly compositional distribution, and crystalline defects are revealed by detailed analyses of EDS, HRTEM and SAED in the circled or uncircled positions shown in Figure 1c. For instance, EDS data suggest Position 2, 7, and 8 show a Cu poor and Zn rich composition, demonstrating Zn tends to segregate at the bottom of the absorber layer. Indexing of SAED patterns show that amorphous Cu_2SnS_3 (*s.p. Cc*) formed at Position 3 and 10 (diffused ring to spotty ring pattern), and $Cu_{7.2}S_4$ (*s.p.* $Fm\bar{3}m$) and SnS (*s.p. Pnma*) segregated at Position 11 (see Figure S4a−c in the Supporting Information), which suggests these regions incompletely reacted with Zn rich phases. Higher sulfurization temperatures will assist in these secondary phases reacting to form kesterite crystals; however, it will inevitably lead to the complete consumption of ITO back contact as shown in Figure S2 in the Supporting Information. Position 6 and 8 feature with stacking faults and display Cu poor and In rich CZTIS phases (seeFigure S4d, e in the Supporting Information). Besides, the EDS result for Position 1 suggests the out-diffusion of Cu into the remnant ITO back contact, which may cause a loss of constituent elements and possibly result in the Cu poor content at Position 2, 7, and 8. Additionally, because of the loss of In into the absorber, the effective thickness of remnant ITO layer is less than 100 nm. Thus, electrical conductivity of the ITO back contact may be inevitably deteriorated by sulfurization.

Figure 2 gives the phase identification of the Cu−Zn−Sn−S precursor and the absorber on ITO substrate via X-ray diffractogram (XRD). For the precursor, there is a very wide peak located at $2\theta \approx 42-43°$ that corresponds well with brass CuZn (PDF 97−005−6276) and bronze CuSn (PDF 97−005−6282) alloys, and the rest peaks can be entirely coming from ITO substrate (PDF 97−005−0849). For the absorber, no reflection from Cu_XS and Cu_2SnS_3 considerably visible in the XRD pattern indicates the content of these phases is very little or they are poorly crystalline. Else, the peak at $2\theta = 15.080°$ corresponds well with the 001 peak of SnS_2 (PDF 97−065−0993), and the intense peaks at $2\theta = 26.179$, 27.475, 31.640, and 31.981°, respectively, correspond to the 201, 210, 301, and 400 peaks of SnS (PDF 97−005−2108), implying tin sulfides present in the absorber layer with a relatively big amount. Given the non-Sn rich composition of the precursor, we can speculate that the diffusion of In substituting Sn leads to form tin sulfides in the absorber. As additionally shown in the insets that display the magnified 112, 024, and 116 reflex, the reflections of CZTIS absorber shift significantly toward lower angles (bigger unit cell size) than CZTS (PDF 97−018−9286). Correspondingly, the obtained lattice parameters of CZTIS absorber, as shown in Table 2, are bigger than kesterite CZTS (*s.p.* $I\bar{4}$) and smaller than chalcopyrite $CuInS_2$ (*s.p.* $I\bar{4}2d$).[17] This is another evidence for substitutional diffusion of In into CZTS absorber. Furthermore, higher sulfurization temperatures will cause more In diffusion into absorber layers with more expanded lattices, as shown by Figure S3 in the Supporting Information. As additionally shown in Figure S3 in the Supporting Information, the nearly congruent interplanar spacing of the film sulfurized at 500 °C with kesterite CZTS suggests In might probably just start to diffuse into the film at 500 °C or the content of diffused In in the film is very little. Besides, the broadening and splitting of the reflections implies the phase segregation in the CZTIS absorber, possibly coming from the agglomerates with different In contents revealed by the TEM analysis (such as Position 6, 7, and 8 in Figure 1c). As compared to chalcopyrite type structure, kesterite produces

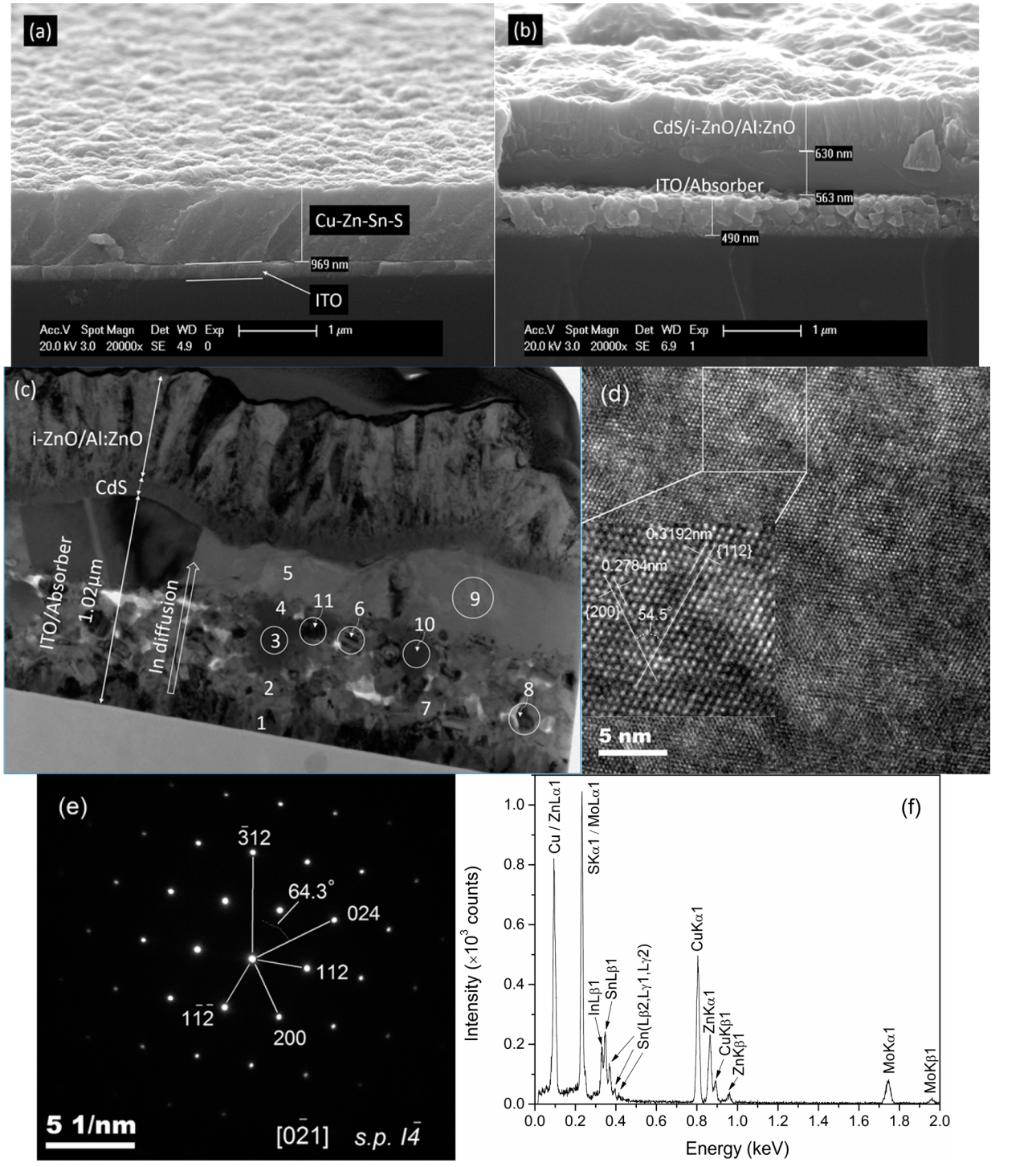

Figure 1. SEM cross-sectional images of (a) coelectrodeposited Cu−Zn−Sn−S precursors on ITO substrate and (b) bifacial device; (c) bright-field TEM images of the bifacial device; (d) HRTEM image, (e) SAED pattern, and (f) EDS profile of CZTIS at Position 9.

additional XRD peaks, such as 002, 110, 114, 006, due to the different orderings of the constituent metallic elements. However, the absence of these visibly intense peaks make it hard to identify the structures (chalcopyrite vs kesterite) of our CZTIS absorber. At least, the observation of a weak 110 reflection demonstrates the presence of kesterite structure in the absorber layer.[18] Meanwhile, the substitutional diffusion of In may invoke the cation disorder, lattice deformation, furthermore, the cancellation of minor reflections (such as 002 reflex),[19] complicating the structure identification. Notably, no ITO peaks observed in the XRD pattern of the solar cell indicates again that ITO back contact has been severely destroyed by the high temperature sulfurization with H_2S gas.[16] As known, because of the multivalency of constituent Sn, CZTS behavior instable and tend to decompose into binary sulfides during the thermal processing. The partial substitution of Sn with the group III element In might, therefore, improve the stability of material because of the more stable III oxidation state and the lower volatility of indium chalcogenides than Sn/Ge.[6,7]

Table 2. Experimental Lattice Constants of CZTIS by Analogy with CZTS and CIS

	interplanar spacing d (nm)			lattice parameters		
	{112}	{024}	{116}	a (Å)	c (Å)	V (Å^3)
CH−CIS[a]	0.3197	0.1960	0.1659	5.523	11.133	339.6
KS-CZTS[a]	0.3126	0.1919	0.1636	5.427	10.868	319.5
XRD[b]	0.3153	0.1932	0.1695	5.461	10.923	325.8
TEM[b]	0.3192	0.1968	0.1688	5.556	10.951	338.0

[a]The lattice parameters of chalcopyrite-$CuInS_2$ (CH−CIS, *s.p.* $I\bar{4}2d$, PDF 97−006−6865) and kesterite-Cu_2ZnSnS_4 (KS-CZTS, *s.p.* $I\bar{4}$, PDF 97−018−9286) are referenced. [b]The spacing values of {112} and {024} were used to calculate the lattice parameters based on the formula of tetragonal lattice structure, $1/d^2 = (h^2 + k^2)/a^2 + l^2/c^2$.

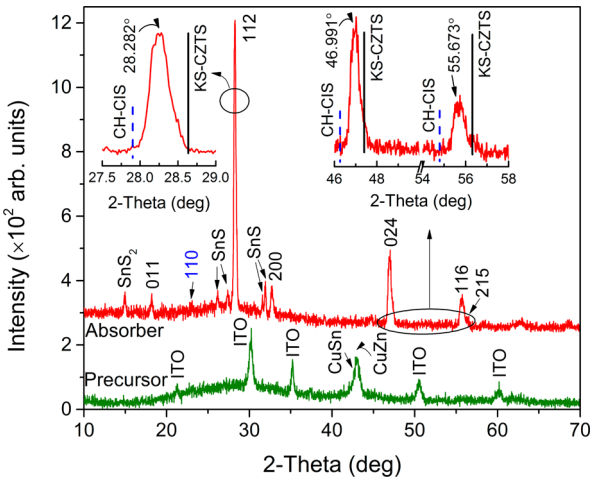

Figure 2. X-ray diffraction patterns of the coelectroplated Cu−Zn−Sn−S precursor on ITO substrate and the absorber film. The zoomed reflections for highlighting. Solid and dash line makers represent the peak positions of KS-CZTS (PDF 97−018−9286) and CH−CIS (PDF 97−006−6865), respectively.

Figure 3 characterizes the absorption properties of the CZTIS absorber layer grown on ITO substrate. As shown in Figure 3a, the high transmission in the infrared region typically suggests the absorber layer is characteristic of lower free carrier absorption and thus high resistance, in sharp contrast to the ITO substrate. This, consistently, demonstrates the conductivity of the ITO substrate has been severely destroyed by the high temperature sulfurization; otherwise, the absorber layer should has remained a lower transmission in the infrared region. The estimated optical absorption coefficient α of the absorber layer in Figure 3b displays the CZTIS alloy has also a strong optical absorption, 3.2 $\times 10^4$ to 1.2 $\times 10^5$ cm^{-1}, in the visible light region, as compared to CZTS,[20−22] although In has one p electron less than Sn. The higher visible light absorption is critical to reach high efficiency cells with a thinner absorber film thickness. Else, as shown in Figure 3c, the CZTIS absorber has the congruent band gap value (E_g) 1.48 eV with kesterite CZTS. For the kesterite CZTS, the valence band maximum (VBM) and the conduction band minimum (CBM) are composed by the antibonding state of Cu-3d/S-3p orbitals and the bonding state of Sn-5s/S-3p orbitals, respectively. In has a higher 5s orbital than Sn, which will result in a higher bonding state of In-5s/S-3p orbitals than Sn-5s/S-3p located inside the conduction band of CZTS. Thus, the partial substitution of Sn with In has no impact on the fundamental band gap structure of kesterite CZTS.[23] Compared to Ge, In substituting Sn may consequently neither increase the E_g of absorber nor reduce the J_{SC} of the cell.

The CZTIS absorber film is further examined using polarized Raman spectroscopy (Figure 4). The Raman spectrum shows the visibly intense peaks, excluding 196.1 and 408.2 cm^{-1}, which correspond well to the vibrational character of kesterite CZTS.[20−22,24] The weak fitted peaks at 196.1 and 408.2 cm^{-1} are still observed in our other CZTS samples on Mo substrate.[25] Thus, we tentatively ascribe these two additional vibrational peaks to the background noises rather than assignable to either the doping of In or the secondary phases. Meanwhile, the Raman measurements detected at different surface regions are identical and representive of the entire film. No spurious phases, such as SnS_2 (315 cm^{-1}), SnS (95, 165, 192, and 220 cm^{-1}), Cu_XS (475 cm^{-1}), and Cu_2SnS_3 (290 and 352 cm^{-1}),[20] were identified by the Raman spectroscopy, suggesting these spurious phases segregating in the bottom absorber layer given the limited penetration depth (~65 nm)[20] of 532 nm laser. On the other hand, the main Raman peak (332.0 cm^{-1}) of CZTIS absorber shows a significant shift to lower frequency than the sulfur breathing mode of kesterite CZTS (335−339 cm^{-1}). This red shift should relate to the lattice expansion, the increased bond length, and thus the reduced force constant (In−S vs Sn−S) of CZTIS as Sn was partially substituted by In.[26] In addition, the measured main Raman peak of CZTIS absorber is characterized by a significant broadness with the full width at maximum of 11.5 cm^{-1}, indicative of a small phonon lifetime and correlation length, while the fitted peak at 301.9 cm^{-1} shows a strong spectral intensity. These phenomena might be attributed to the presence of significant cation disorder effects (i.e., the higher densities of lattice defects and lower symmetry of crystalline structure) that promote additional phonon scattering in the quinary CZTIS alloy as compared to ordered kesterite CZTS.[24]

As stated afore, the oxidation multistates of Sn can create deep recombination centers in CZTS and damage the device efficiency. The partial substitution of Sn with In might, therefore, positively alleviate the deep defects due to its stable III oxidation state. In order to understand the defect distribution in the In substituted CZTS absorber layer, the excitation- and temperature-dependent photoluminescence (PL) studies at low temperature are presented in Figure 5. The observed PL spectra feature with the asymmetric broadbands with the intensity maxima at 1.105−1.125 eV. These PL emission peak energy maxima are much lower than the plotted optical band gap ~1.48 eV, and slightly smaller than the corresponding reported values 1.14−1.3 eV as well.[27−31] The dependence of the integrated PL intensity (I_{PL}) on the excitation intensity (P_{exc}) for this transition band is found to obey the expression

$$I_{PL} \propto P_{exc}^{m} \quad (1)$$

where m is a characteristic parameter usually ranging between 0.5 and 2. Values of $m > 1$ are expected for the transitions of excitons or band-to-band, whereas $m \leq 1$ are expected for the transitions involving defects (donor−acceptor pairs (DAP) ($m < 1$) or free to bound (FB) transitions ($m = 1$)). A fit using eq 1 yields m value of $m = 0.902 \pm 0.043$. It is an indicator that this emission has a partial characteristic of classical DAP transition. Additionally, the PL excitation intensity generally has an exponential relationship with the emission peak energy (E_P), namely,

$$P_{exc} = P_0 e^{E_P/\beta} \quad (2)$$

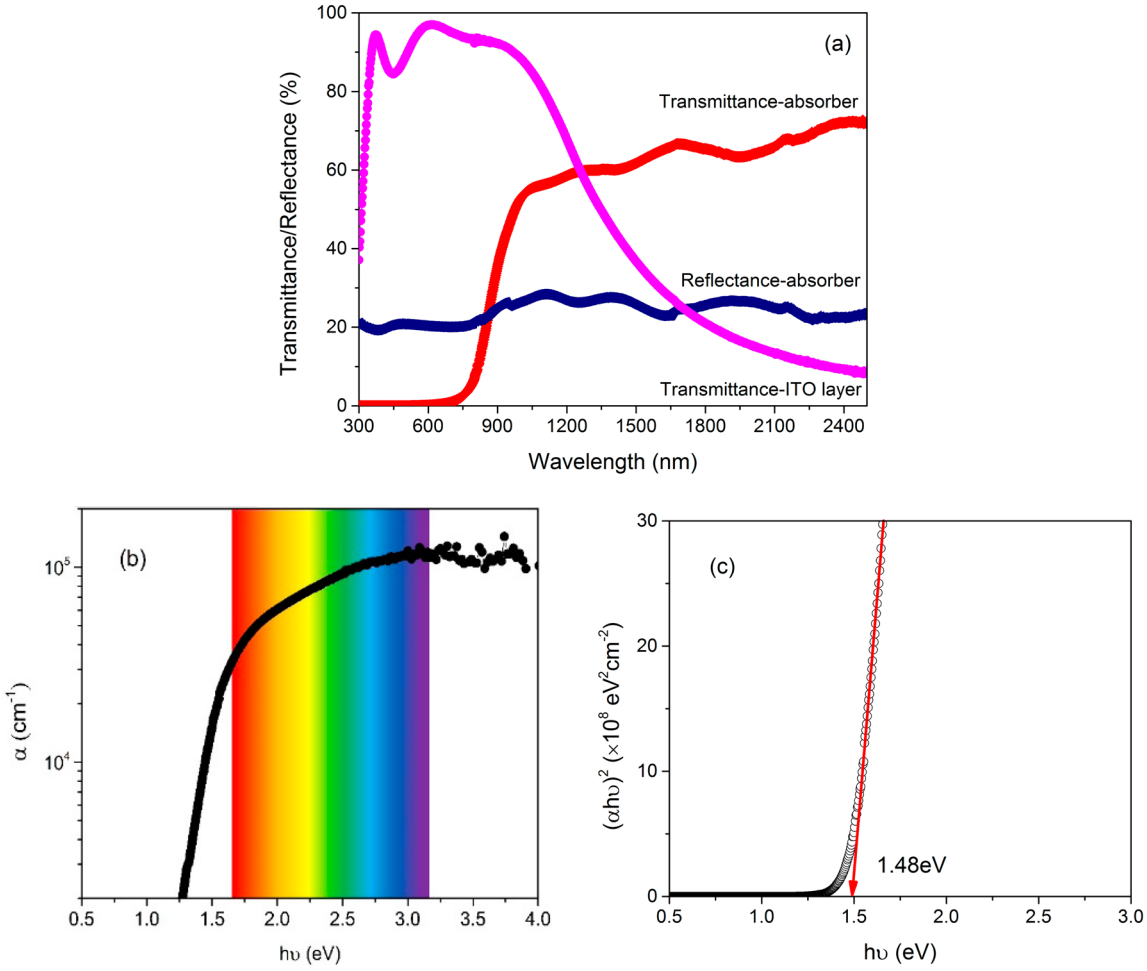

Figure 3. (a) Optical transmission and reflectance of the CZTIS absorber plus the transmission of ITO substrate, (b) the absorption coefficient α, and (c) the plot of band gap energy of the CZTIS absorber. The absorption coefficient (α) was extracted from the transmission and reflectance of the absorber layer based on the relation, $\alpha = -1/d[((1-R)^2 + ((1-R)^4 + 4T^2R^2)^{1/2})/(2TR^2)]$,[20,21] where the effective film thickness d takes 850 nm. The band gap energy of the absorber layer was estimated using the plot of $(\alpha h\upsilon)^2 \sim h\upsilon$ as a direct-gap semiconductor with ideal parabolic bands, where $h\upsilon$ is the photon energy.

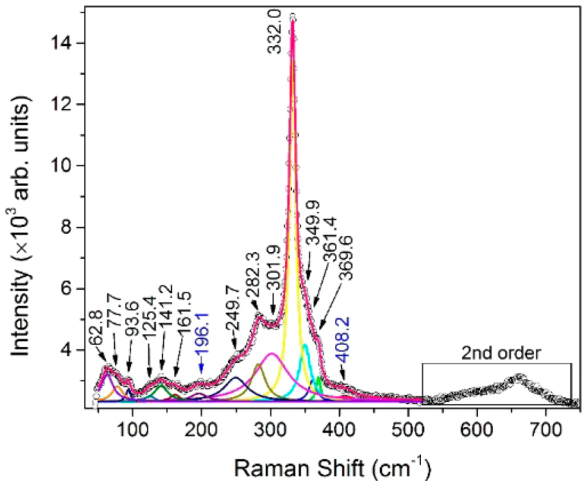

Figure 4. Raman spectrum of the CZTIS absorber, with the peaks being fitted using the Lorentzian curves.

where P_0 is a coefficient and β is defined as the energy-shift constant.[32−35] Typically, the values of β are found to be around 1−4 meV for the classical DAP and zero for FB, however, the fitted β value by eq 2 (β = 10.70 ± 0.74 meV) is much higher. This drastic blue shift in energy for kesterite can most readily be understood in the context of electrostatic potential fluctuations rather than the classical DAP related in the purely uncompensated or weakly compensated materials.

Potential fluctuations are usually associated with highly compensated and heavily doped materials, where the randomly distributed charged impurities with a much larger amount cannot be screened by the lower free-carrier density. Such spatial fluctuations will blur the band edges, thus broaden the defect levels, and eventually form band tails. They also strongly influence the optical and electrical properties as new transitions with significantly smaller transition energy, lower-energy tails of luminescence, and bigger energy-shift constant (β) than the standard DAP model become possible. However, the excitation- and temperature-dependent luminescence intensity in the case of fluctuating potentials may be congruent with classical DAP model. It, thereby, was called as quasi-DAP (QDAP).[32,33]

The average depth of the fluctuations, γ_0 (Figure 5c inset), can be estimated from the average charge fluctuations occurring within a certain volume defined by the screening radius $r_s = N_I^{1/3} p^{-2/3}$ containing an impurity concentration $N_I = N_A^+ + N_D$ screened by a hole concentration $p = N_A - N_D$ (not necessarily the free ones) for p-type material,[33−35] namely

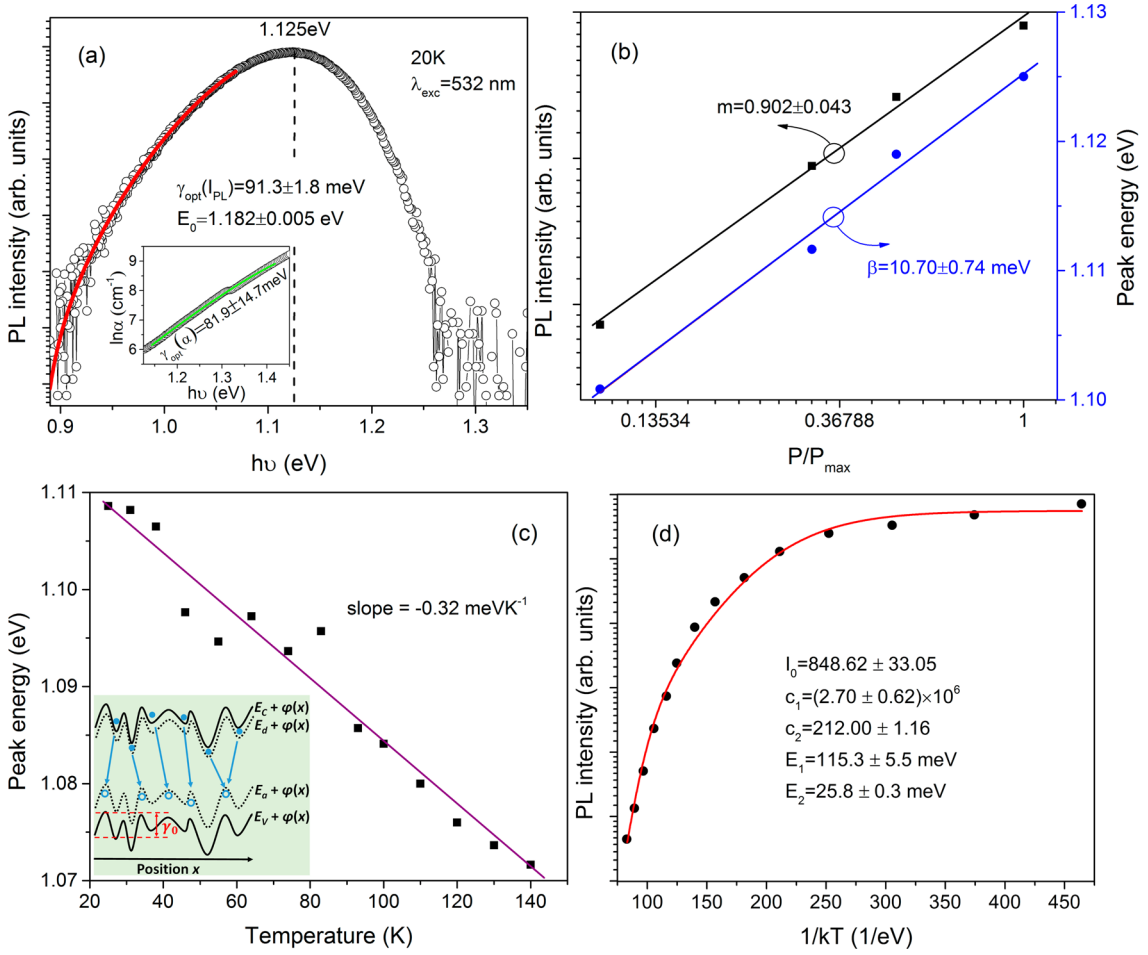

Figure 5. (a) PL spectrum of CZTIS absorber (red line fitted to eq 4); inset, estimation of γ_{opt} from eq 5; (b) excitation-dependent PL integrated intensity and peak maxima at 20 K (linear fitting to eq 1 and 2), (c) temperature-dependent PL integrated intensity (red line fitted to eq 7) and (d) peak maxima. The PL intensities are plotted on a natural logarithmic scale in panels a, b, and d. (c, inset) Effect of potential fluctuations on the band edges and the irradiative transitions between trapped electrons and holes, where $\varphi(x)$ represents the spatial varying electrostatic potential due to the potential fluctuations and the dashed line represents an acceptor/donor level or band.

$$\gamma_0 = \frac{q^2}{4\pi\varepsilon_r\varepsilon_0}\frac{(N_I r_s^3)^{1/2}}{r_s} = \frac{q^2}{4\pi\varepsilon_r\varepsilon_0}\frac{N_I^{2/3}}{p^{1/3}} \quad (3)$$

where q, ε_r, and ε_0, is the elementary charge, the static and vacuum dielectric constant, respectively. Usually, the value for γ_0 is expected as large as the degree of compensation of the doped materials and proportional to the energy-shift constant β. In the heavily doped and highly compensated materials, N_I and p are thought to rely less on the temperature. Thus, the γ_0 determined at lower temperatures also conforms to room temperature. On the other hand, γ_0 varies inversely with the excitation intensity, because the number of carriers available for screening can be boosted under higher excitation intensity whereas N_I approximately does not changes.

Likewise, the edge luminescence spectral intensity for the heavily doped and highly compensated materials relates with the excitation intensity.[36] For high photoexcitation intensities, the decay of I_{PL} at low energies reproduces the behavior of the absorption coefficient as described in eq 5, i.e. $I_{PL} \propto \alpha$. For the very low photoexcitation intensities, the decay of I_{PL} at low energies can be treated defect-likely as a Gaussian shape:

$$I_{PL} \propto \exp\left(-\frac{(h\upsilon - E_0)^2}{2\gamma_{opt}^2}\right) \quad (4)$$

where E_0 is the average energy of the transition bands in the case of fluctuation potentials. A well coincidental fit using eq 4 to the asymmetric PL emission at low energies as shown in Figure 5 a yields E_0 = 1.182 ± 0.005 eV and $\gamma_{opt}(PL)$ = 91.3 ± 1.8 meV. Optical transitions in the fluctuating potentials are assisted by tunneling due to the spatial separation of nonequilibrium carriers (i.e., holes and electrons) localized by the potential wells. Usually, the tunneling length of the optical transition (r_t) is smaller than the screen length of potential fluctuation (r_s), the fluctuation amplitude relevant for optical processes γ_{opt} is, therefore, less than γ_0.

Also, the optical absorption spectrum provides another direct access to γ_{opt}. Using the model proposed by Shklovskii and Efros,[34,37,38] the absorption coefficient (α) could be expressed with a 5/4 exponential dependence on the photo energy ($h\upsilon$) in the presence of significant screening for highly compensated materials

Table 3. Device Parameters for the Bifacial CZTIS Cell under Front, Rear, and Bifacial Illumination and in Dark[a]

	eff. (%)[b]	FF (%)	V_{OC} (mV)	J_{SC} (mAcm^{-2})	$R_{S,\,L}$ (Ω)	$R_{sh,\,L}$ (Ω)	$R_{S,\,D}$ (Ω)	$R_{sh,\,D}$ (kΩ)	E_g/q-V_{OC} (V)
front	2.9	40.7	489.3	14.6	195	2120	87	426	0.99
rear	1.3	41.6	427.6	7.1	326	4554			1.05
bifacial	3.4	39.3	461.1	18.8	169	1640			1.02

[a] $R_{S,\,L}$, $R_{sh,\,L}$, $R_{S,\,D}$, and $R_{sh,\,D}$ are the series resistance in light, shunt resistance in light, series resistance in dark and shunt resistance in dark conditions, respectively. E_g/q-V_{OC} presents the V_{OC} deficit, q being the elementary charge, E_g the band gap value of the absorber and V_{OC} the open circuit voltage of the cell. Cell area is 0.07 cm^2. [b] The efficiencies were entirely calculated from one sun light intensity. Note: the effective light intensity incident on the front *p-n* junction varies with illumination modes, following by bifacial > front > rear, due to the absorption loss arising from the bottom absorber layer at the back junction and ITO substrate.

$$\alpha \propto \exp\left(-\frac{2}{5\sqrt{\pi}}\left(\frac{E_g - h\upsilon}{\gamma_{opt}/2}\right)^{5/4}\right) \tag{5}$$

which allows us to determine γ_{opt} by fitting the absorption spectra (Figure 3b). A fit to data is shown in Figure 5a inset where the data below E_g (i.e., 1.48 eV) were utilized to estimate γ_{opt}. The fitted γ_{opt} of the absorption spectrum, $\gamma_{opt}(\alpha) = 81.9 \pm 14.7$ meV, is basically on par with that of the PL intensity ($\gamma_{opt}(PL)$). The obtained γ_{opt} values of CZTIS alloy, 30−40 meV bigger than CZTSSe alloy and CZTS powder samples,[36,37] suggests that In alloying probably has a great effect on the band tail defect distribution. Large γ_{opt} predicts severe band tailing from electrostatic potential fluctuations and therefore negatively impacts on V_{OC}.

Furthermore, replacing the screen length of potential fluctuation r_s in eq 3 with the tunneling length of the optical transition $r_t = \hbar/(m_r^*\gamma_{opt})^{1/2}$ gives the relation between γ_{opt} and N_I, namely

$$\gamma_{opt}^5 = \left(\frac{q^2}{4\pi\varepsilon_r\varepsilon_0}\right)^4 \frac{N_I^2\hbar^2}{m_r^*} \tag{6}$$

where m_r^* is the reduced effective mass of the material.[34] Using the fitted γ_{opt} values by PL and absorption spectra, the total impurity concentration N_I can be calculated by eq 6 to be around 6.5−7.2 × 10^{19} cm^{-3} with the assumption that CZTIS alloy has the congruent physical constants (ε_r, m_r^*) with pure CZTS.

Figure 5c, d display the dependence of the peak position and intensity on temperature. The peak energy shifts to smaller energies (redshift) with a gradient of 0.32 meV K^{-1} as the temperature increases. This behavior is another unique signature of potential fluctuations (QDAP), whereas DAP transition usually shows a slight blueshift. The temperature-dependent PL intensity of QDAP can be simply expressed as a biexponential relation, namely,

$$I_{PL} = I_0/(1 + c_1 e^{-E_1/kT} + c_2 e^{-E_2/kT}) \tag{7}$$

where I_0 is the intensity extrapolated to 0 K, k is the Boltzmann constant, $c_{1,\,2}$ are the parameters proportional to the degeneracy factor ratio between the corresponding level and ground state, and $E_{1,\,2}$ represents the characteristic activation energies of acceptor/donor.[31] An analysis of the PL intensity in Figure 5d using eq 7 yields activation energies of approximate 25.8 and 115.3 meV. Although the errors are relatively large, it can be concluded that a deep level at E_1 = 115.3 meV and a shallow level at E_2 = 25.8 meV participate in the observed transition. However, we have to caution that the interpretation of transition energies and their temperature-dependence is difficult in the presence of potential fluctuations, as thermal redistribution processes within the potential well landscape occur. Given the formation of charged defects with a large number, such as In_{Sn}^{-} and V_S^{2+}, it is reasonable to match them with the plotted $E_{1,\,2}$, but there still exist a lot of uncertainties to identify by theory. First, the activation energy of V_S^{2+} has a distinct discrepancy in the theoretical results for CZTS: Chen et al. report it is a deep midgap donor;[39] however, Sun et al. assume it does not introduce any transition levels in the band gap.[40] Second, the likely existence of Cu_{Sn}^{3-}, Zn_{Sn}^{2-}, or V_{Sn}^{4-} in CZTIS, which are proved to be deep acceptors in CZTS,[39] might possibly participate in PL emission. Third, it is also likely to create new deep levels or make the intrinsic levels deeper as Sn is gradually substituted by In, because of the discrepancy of binding energies of In and Sn.

The emission peak energy for QDAP transition (E_{QDAP}) is thought to obey the expression below:

$$E_{QDAP} \approx E_{DAP} - 2\gamma_0 \approx E_g - (E_d + E_a) - 2\gamma_0 \tag{8}$$

where E_{DAP} is the emission peak energy for DAP transition; $E_{d,\,a}$ is the characteristic activation energy of donor and acceptor, respectively.[32] Using the peak energy E_{QDAP} = 1.125 eV at 20 K, E_1 = 115.3 meV, E_2 = 25.8 meV and E_g = 1.55−1.60 eV for 20 K,[41] we can obtain the average depth of the fluctuations γ_0 = 141−167 meV from eq 8. Followed by substituting γ_0 = 141−167 meV and N_I = 6.5−7.2 × 10^{19} cm^{-3} into eq 3, the hole density of CZTIS can be roughly estimated to be p = 1.8−0.9 × 10^{19} cm^{-3}. This enhanced hole density bigger than pure CZTS (1 × 10^{16} to 1.5 × 10^{18} cm^{-3})[28,31,42] is expected capably to boost the build-in potential and thus V_{OC} of the device.

The electrical J−V characterization in Figure 6 shows the performance of the best bifacial mini cell, with the corresponding device parameters under light and dark conditions listed in Table 3. Specifically, this cell shows an enhanced power conversion efficiency of 3.4% under bifacial illumination. However, the cell suffers from the large V_{OC} deficits (E_g/q-V_{OC}) as high as approximate 1 V, large light/dark series resistances ($R_{S,\,L}$ and $R_{S,\,D}$), and low fill factors (FF). Besides, the electrical parameters under different illumination modes (rear, front and bifacial) show significant light-intensity related features. $R_{S,\,L}$ decreases from through rear, front, to bifacial illumination, which is likely due to the improved photoconductivity of the CdS layer. The varied shunt resistances ($R_{sh,\,L}$ and $R_{sh,\,D}$) under different illumination modes manifests the parasitic effect in the cell. The V_{OC} for bifacial illumination shrinks as compared to front illumination, rather than increases.[13] This abnormal behavior is impossibly due to neither the pinning of the Fermi level nor the temperature effect. Actually, it may be understood in the case of a nonohmic (Schottky-like) back contact which produces a diode of opposite polarity as the front diode (CdS/CZTIS heterojunction) as shown in Figure 6d inset.[43,44] When the light illuminated from the rear side, the back junction would produce more negative photovoltaic voltage and cause the shrinkage of net V_{OC}. Besides, the variance of FF under different

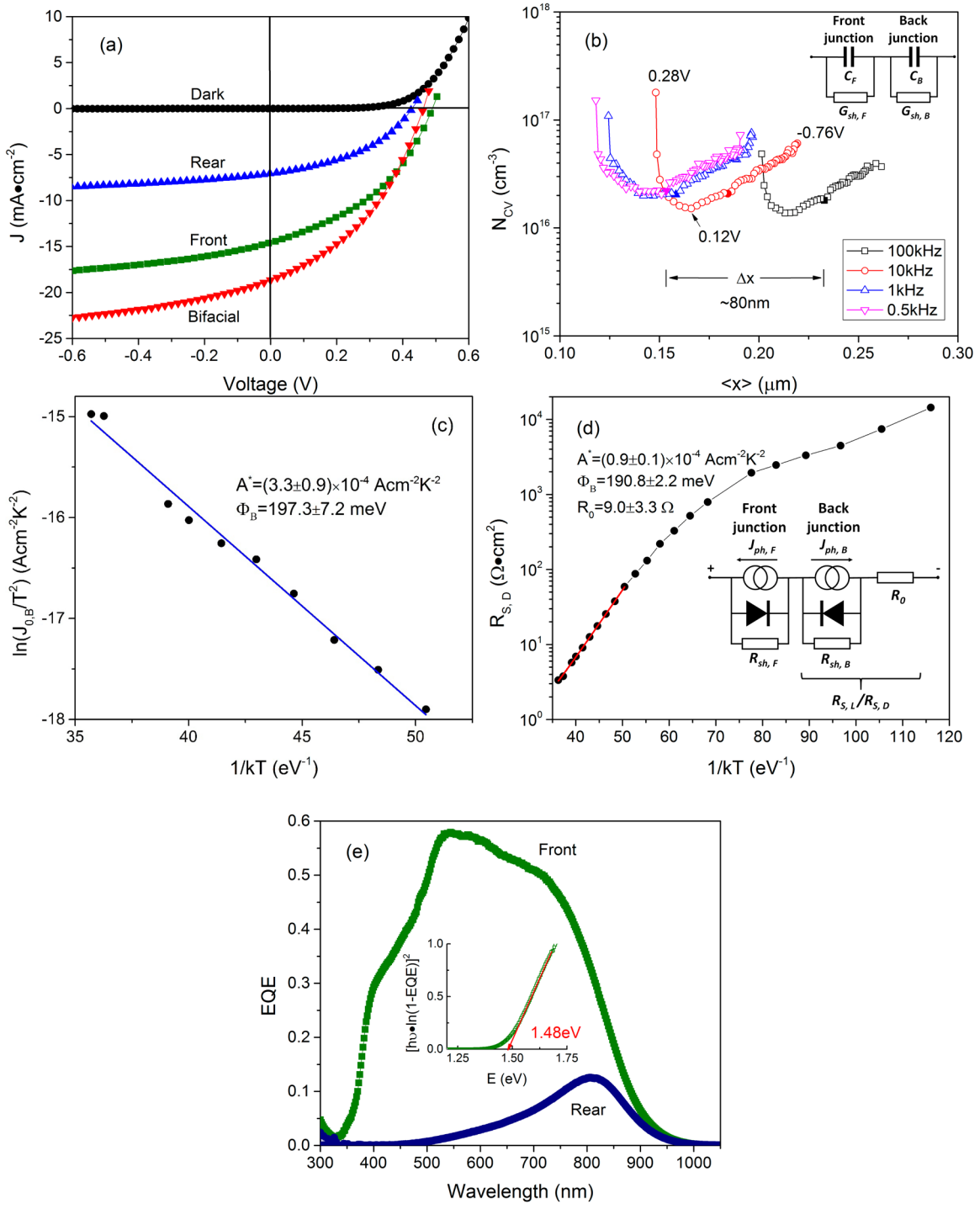

Figure 6. (a) Electrical characterization of the bifacial device: the electrical $J-V$ curves under dark and light (rear, front, and bifacial illumination); (b) the frequency dependent net charge carrier profiles calculated from the $C-V-f$ scans for the solar cell (solid symbols correspond to the N_{CV} calculated at 0 V; $\langle x \rangle$ is the distance from junction); (c) the Arrhenius plot of $J_{0,B}(T)$ yielding the barrier height; (d) temperature dependence of dark series resistances $R_{S,D}(T)$ (red line fitted to eq 12); (e) the EQE curves under front and rear illumination and band gap estimation, and the sketches of (b, inset) AC and (d, inset) DC equivalent circuits of the solar cell. Note: in AC equivalent circuit, capacitance denotes the imaginary part of the complex admittance divided by $2\pi f$, and conductance denotes the real part of admittance. The static dielectric constant of $\varepsilon = 6.7$ was used to calculate the net charge carrier concentration (N_{CV}) and the profiling depth ($\langle x \rangle$).

illumination modes tends similar to V_{OC} as well.[45] The plotted γ_{opt}, in fact, is of the same magnitude the well performed CZTSSe solar absorber.[46] Thus, it can be concluded that the band tailing is not the limiting factor for large V_{OC} deficit, whereas the nonohmic back contact should primarily account for the very low V_{OC} and FF of the bifacial device. On the other hand, the shunt resistance at the back contact ($R_{sh,B}$) is physically associated with the poor regions of the back junction, thus, its value should be lower and leads to the current leakage of the back junction.[47] Otherwise, the current of bifacial device would be blocked by the back barrier and consequently cause the shrinkage of J_{SC} and the severe rollover of $J-V$ curves.

Figure 6b depicts the net charge carrier profiles of the cell that were derived from capacitance−voltage scans with different frequencies ($C-V-f$) of the AC signal (f = 0.5, 1, 10, and 100 kHz), and the AC equivalent circuit is given in the inset. These profiles have an almost identical shape, however, only shift by a distance Δx. Regarding to the profile at 10 kHz, N_{CV} takes a minimum value at 0.12 V bias, increases sharply toward larger forward bias side (0.28 V), and grows gradually to the reverse bias side (−0.76 V). Overall, the charge carrier profiles reveal a nonuniform spatial distribution of impurity density. At reverse and lower forward bias, the back junction will not share voltage with the front junction CdS/CZTIS, so the measured capacitance equals to the capacitance of front junction (C_F). The observed gentle growth of N_{CV} toward the bulk of the absorber (reverse bias) for each frequency, therefore, is probably due to either substitutional diffusion of In that might cause the discrete or continuous distribution of deep traps, or a nonuniform thickness of the absorber. Seeing the mean values of the net charge carrier density N_{CV} biased at 0 V 2.19×10^{16} cm^{-3} (0.5 kHz), 2.06×10^{16} cm^{-3} (1 kHz), 2.00×10^{16} cm^{-3} (10 kHz), 1.60×10^{16} cm^{-3} (100 kHz), we find N_{CV} decreases slightly as the measurement frequency increases. It manifests the deep traps contributable to the C−V signal due to the lower capture and emission rates at lower frequencies.[48] As the forward bias increase, the back junction will start to limit the current and share both the DC bias and AC signal voltage with the front junction. This will consequently reduce the measured capacitance to the series connection of the capacitances of front junction C_F and back junction C_B ($C_{total} = C_B C_F/(C_B + C_F)$), or just C_B if the bias was high enough, contributing to the sharp increase of N_{CV} under larger forward bias.[49−51] Likewise, the measured capacitance of the cell also respond to different measuring frequencies: for high frequencies ($\omega \gg (G_{sh,F} + G_{sh,B})/(C_F + C_B)$), the total capacitance reduces to $C_{total} = C_B C_F/(C_B + C_F)$; for low frequencies ($\omega \ll (G_{sh,F} + G_{sh,B})/(C_F + C_B)$), the total capacitance equals to C_F. This will contribute to the profiling distance shift (Δx) for the different measuring frequencies. The distance shift $\Delta x \approx 80$ nm between the profiles of 100 kHz and 0.5 kHz actually relates to the variance in depletion width of the back junction,[49] which in turn depends on the barrier height and the impurity density of the bottom absorber layer with the depletion region of back junction.

Actually, this nonohmic back contact was proved to prevail with our bifacial devices (∼50 mini cells) that entirely show a reduced V_{OC} under bifacial illumination. Some of them were revealed to have much higher barrier heights evidencing by the double capacitance maxima in $C-V-f$ curves and larger profiling distance shifts (Δx).[52−54] The formation of ohmic contacts to p-type CZTIS/CZTS is difficult owing to the high electron affinity (4.5 eV) and large band gap (1.5 eV), meaning that a metal or degenerated TCO of work function 6.0 eV is required. Most metal contacts to CZTS therefore form a Schottky barrier at the back contact.[55,56] ITO was demonstrated to make good devices with low band gap CIGS (E_g = 1.1 eV), however, it is not valid for high band gap CIGS (E_g > 1.35 eV).[13,14] Theoretically, other TCO electrodes, such as SnO_2 and ZnO, should not be competent for the ohmic back contact due to the decreasing VBM with increasing band gap, even with respect to the low band gap CIGS. However, in the case of sufficient interface states or midgap states in the TCO, defect-assisted tunneling and recombination merit forming ohmic contact, even for wider band gap CGS.[13] Our bifacial devices do not display a well-performed ohmic contact, even though the metallurgical reaction between absorber and ITO back contact resulted in a problematic bottom layer of absorber full with various defects, which together with the high doping of absorber by In should have made it easier to form ohmic contact; conversely, it is not the case. On one aspect of the problem, the interfacial reaction may very likely change the electronic properties of ITO in terms of Cu/S doping, Sn/O removals, or other factors. This will consequently reduce its work function, negative for ohmic contact. On the other hand, the lack of sufficient paths for tunneling and recombination, such as interface states or midgap states in the back barrier or ITO, could be very likely responsible for the nonohmic back contact as well. In addition, the profiling distance shift (Δx) of CV related to the width of the back barrier is as high as 80 nm, which is still challenging for the direct tunneling of back barrier (<10 nm)[57] if without the assistance of sufficient trap states in the barrier. In such case, the thermionic emission may still dominate the passage of carriers over the back barriers at higher temperatures. Conversely, the tunneling process will be dominant at lower temperatures.

To access the barrier height at back contact of the bifacial device, the dark $J-V$ measurements as a function of temperature: $J-V-T$ measurement was conducted.

$$J_{D,B} = J_{0,B}\exp\left(\frac{qV_B}{n_{B,D}(T)kT} - 1\right) \tag{9}$$

where $J_{0,B}$, $n_{B,D}(T)$, and V_B are, respectively, the saturation current density, ideality factor, and the voltage drop across the back junction in dark.[58,59] Moreover, the saturation current density can be expressed as

$$J_{0,B} = A^* T^2 \exp\left(\frac{-\Phi_B}{n_{B,D}(T)kT}\right) \tag{10}$$

where A^* is the effective Richardson constant and Φ_B is the barrier height of the back contact, both of which are weakly temperature dependent. The contact resistance coming from the nonohmic back contact $R_{S,B}$ can be derived by differentiating eq 9, $R_{S,B} = \partial V_B/\partial J_{D,B}$ at zero bias, namely

$$R_{S,B}(T) = \frac{k}{qA^*T}\exp\left(\frac{\Phi_B}{n_{B,D}(T)kT}\right) \tag{11}$$

Equations 9 and 10 can be used to evaluate Φ_B and $R_{S,B}$, if $n_{B,D}(T)$ was known. With little or no tunneling current or depletion-layer recombination, $J_{0,B}$ is determined by that of thermionic emission and $n_{B,D}(T)$ is close to unity. For higher doping and/or lower temperature, tunneling starts to occur and both $J_{0,B}$ and $n_{B,D}(T)$ increase.[60] Hereafter, $n_{B,D}(T)$ is supposed to be unity for the determination of desired parameters.

The saturation current density $J_{0,B}$ of the back contact can be approximately obtained from the intercept point of the prerollover and postrollover (see Figure S5 in the Supporting Information).[61,62] The Arrhenius plot of $\ln(J_{0,B}/T^2) \sim 1/kT$ (325−230 K) then yields $\Phi_B = 197.3 \pm 7.2$ meV and $A^* = (3.3 \pm 0.9) \times 10^{-4}$ A cm^{-2} K^{-2} as shown in Figure 6c. Thus, the series resistance coming from the back contact at 300 K can be calculated using eq 10, $R_{S,B} \approx 25$ Ω. At 300 K, the device series resistance $R_{S,D} \approx 82$ Ω. The difference of the two resistances actually corresponds to the background series resistance R_0 because of top/back contact and absorber bulk resistance, $R_0 \approx 57$ Ω. Such a large value of background series resistance is impossibly due to the AZO window layer and the upper layer of

the absorber.[56] At the back contact region, there prevail the small particulates with numerous crystallographic defects that will produce a high density of electronic localized states in the band gap. These local states with a higher density near the individual grain boundaries may be quasi- continually distributed without being fully occupied and thus provide the channel to the carriers.[63] Thus, these small particulates will be very conductive along the grain boundaries and will not increase the series resistance of the device. This is also supported by the well performed kesterite devices which still have very small series resistances despite the presence of particulate-like bottom absorber layer.[64−66] Thus, the degraded ITO back contact should account for the large background series resistance, rather than the bottom absorber layer. The large series resistance of the bifacial device should originate from the existence of the nonohmic back contact and the degraded conductivity of the ITO substrate. On the other hand, higher sulfurization temperatures will lead to the less conductive ITO back contacts, consequently the larger series resistances and the more degraded cell performance as shown in Table S1 in the Supporting Information. In addition, the large series resistance ultimately results in the lowering of FF.

In parallel, another method to access the back barrier is provided by fitting the temperature-dependent series resistance $R_{S,D}(T)$, which can be expressed as

$$R_{S,D}(T) = R_0 + R_{S,B}(T) = R_0 + \frac{k}{qA^*T}\exp\left(\frac{\Phi_B}{kT}\right) \quad (12)$$

where the series resistance $R_{S,D}(T)$ is assumed to be composed of two components: back junction resistance $R_{S,B}(T)$ and background series resistance R_0. $R_{S,D}(T)$ given in Figure 6d were extracted from the J-V-T curves with the standard diode equation (see Figure S5 in the Supporting Information). At low temperatures (<230 K), the bulk resistance of absorber primarily contributes to the high $R_{S,D}(T)$ of the device.[67] At this temperature range, the increase of $R_{S,D}(T)$ actually corresponds to that of the bulk conductivity of CZTIS, suggesting that the highly doped CZTIS absorber layer is nondegenerated. For higher temperatures, the resistance arising from the back contact $R_{S,B}(T)$ will dominate the series resistance, which is in turn determined by the barrier height Φ_B. A good fit to eq 12 using the data from 325 to 230 K yields the effective Richardson constant $A^* = (0.9 \pm 0.1) \times 10^{-4}$ A cm^{-2} K^{-2}, the barrier height Φ_B = 190.8 ± 2.2 meV and the background series resistance $R_0 = 9.0 \pm 3.3\ \Omega$. The series resistance arising from the back barrier at 300 K is $R_{S,B} \approx 72\ \Omega$. The plotted barrier height agrees well with the previous one from the Arrhenius plot, however, the values of $R_{S,B}$ and R_0 are different from the previous ones. The differences in $R_{S,B}$ and R_0 from the two methods should rely on the discrepancy of the Richardson constants A^*. Nonetheless, the plotted Richardson constants ~1×10^{-4} A cm^{-2} K^{-2} are entirely very small, indicating the thermionic emission may be not dominant in the carrier passage over the back barrier. This is very possibly related to the temperature-dependent ideality factor of the back junction $n_{B,D}(T)$, the inhomogeneous back barrier and/or the existence of tunneling process.[56,58,59] The tunneling process may be accounted for the presence of either trap states in the back barrier and/or a very thin insulating layer between ITO back contact and semiconductor due to the detrimental interfacial reaction.

Figure 6e shows the EQE curves under front and rear illumination for the bifacial cell. The band gap were estimated to be 1.48 eV, consistent with Figure 3c, from the front illuminated EQE using the plot of $[h\upsilon \times \ln(1 - \mathrm{EQE})]^2 \sim h\upsilon$ (photon energy). The front EQE curve is inclined toward large wavelengths, due to a small collection function in the bulk of the absorber. This implies the high recombination rates at the problematic absorber bottom layer and back contact. Otherwise, the high series resistance may put the main junction under forward bias, consequently reducing the width of the space charge region with interface recombination setting in and thus resulting in lower EQE. For the rear illumination, the EQE shows a very weak response overall the wavelengths, particularly in the short wavelength region (300−500 nm). This should be related to the presence of the strong absorption and recombination loss at the rear interfacial layer accounting for inadequate photogenerated carriers reaching the space-charge region and short minority carrier lifetime. Low minority carrier lifetime negatively contributes to the lower V_{OC}, FF, and QE response, thus lower J_{SC}.

CONCLUSIONS

In summary, a novel kesterite bifacial solar cell fabricated by H_2S postsulfurization of coelectroplated Cu−Zn−Sn−S precursors has been presented, with an improved efficiency of 3.4% under bifacial illumination relative to those under single-side illuminations (2.9%-front; 1.3%-rear). We have identified an aggressive reaction at the interface between CZTS absorber and ITO back contact due to the intrinsic instable specialty of CZTS. This interfacial reaction accounts for the absorber being stratified with the substitutional diffusion of In into CZTS. The upper absorber layer is constructed with a well crystalline CZTIS alloy, $Cu_{2.040}Zn_{1.000}(Sn_{0.493},In_{0.447})S_{3.677}$, with a sulfur and tin deficient composition. Moreover, the CZTIS alloy is identified to have expanded lattice constants, almost identical optical absorption and similar lattice vibrational properties by analogy with kesterite CZTS. This alloy also shows the nondegenerated and highly compensated characteristic and the severe band tailing. Indium in Group III as a new dopant to CZTS is assumed to capably improve the structural stability and alleviate the deep states due to its stable oxidation state. Importantly, it promisingly merits to increase the hole density and mobility, which will in turn improve the build-in potential and the V_{OC} deficit issue that the kesterite solar device suffers from. Nevertheless not as expected, the nonohmic back contact with ITO substrate is the primary factor limiting the V_{OC} and fill factor of the bifacial device. Else, our results suggest two important factors contributing to the large device series resistance are the existence of nonohmic back contact and the degradation of ITO conductivity due to the interfacial reaction. We have addressed in this work a series of characterizations for the detrimental interfacial reaction, the new CZTIS absorber alloy and the novel bifacial device performance. To gear the kesterite bifacial device toward higher efficiencies, appropriate rear surface passivation techniques should be applied imminently to suppress or alleviate the interfacial reaction and to reduce the extent of nonohmic behavior at the back contact.

ASSOCIATED CONTENT

Supporting Information

SEM, XRD, and TEM data of the CZTIS thin films. The photo and J-V data of bifacial device. This material is available free of charge via the Internet at http://pubs.acs.org/.

AUTHOR INFORMATION

Corresponding Authors

*E-mail: Jie.Ge@UToledo.edu.
*E-mail: jhchu@mail.sitp.ac.cn.

Notes

The authors declare no competing financial interest.

ACKNOWLEDGMENTS

The financial supports by the Knowledge Innovation Program of the Chinese Academy of Sciences (Y2K4401DG0), the National Science Foundation of USA (che-1230246) and the National Natural Science Foundation of China (61474045) are acknowledged. The discussion with Dr. Wan-Jian Yin is also thanked.

DEDICATION

This manuscript is dedicated to Prof. & Dr. Jun-Hao Chu on the Occasion of His upcoming 70th birthday in 2015.

REFERENCES

(1) Wang, W.; Winkler, M. T.; Gunawan, O.; Gokmen, T.; Todorov, T. K.; Zhu, Y.; Mitzi, D. B. Devices Characteristics of CZTSSe Thin-Film Solar Cells with 12.6% Efficiency. *Adv. Energy Mater.* **2014**, *4*, 1301465.

(2) Hiroi, H. Over 12% Efficiency $Cu_2ZnSn(Se,S)_4$ Solar Cell Via Hybrid Buffer Layer. In *40th IEEE Photovoltaic Specialists Conference*; IEEE: Denver, CO, 2014; .

(3) Hiroi, H. Sakai, N.; Kato, T.; Sugimoto, H. High Voltage Cu_2ZnSnS_4 Submodules by Hybrid Buffer Layer. In *39th IEEE Photovoltaic Specialists Conference*; IEEE: Tampa Bay, FL, 2013; pp 0863–0866.

(4) Repins, I.; Beall, C.; Vora, N.; DeHart, C.; Kuciauskas, D.; Dippo, P.; To, B.; Mann, J.; Hsu, W.-C.; Goodrich, A.; Noufi, R. Co-evaporated $Cu_2ZnSnSe_4$ Films and Devices. *Sol. Energy Mater. Sol. Cells* **2012**, *101*, 154–159.

(5) Biswas, K.; Lany, S.; Zunger, A. The Electronic Consequences of Multivalent Elements in Inorganic Solar Absorbers: Multivalency of Sn in Cu_2ZnSnS_4. *Appl. Phys. Lett.* **2010**, *96*, 201902.

(6) Bag, S.; Gunawan, O.; Gokmen, T.; Zhu, Y.; Mitzi, D. B. Hydrazine-Processed Ge-Substituted CZTSe Solar Cells. *Chem. Mater.* **2012**, *24*, 4588.

(7) Hages, C. J.; Levcenco, S.; Miskin, C. K.; Alsmeier, J. H.; Abou-Ras, D.; Wilks, R. G.; Bär, M.; Unold, T.; Agrawal, R. Hydrazine-Processed Ge-Substituted CZTSe Solar Cells. *Prog. Photovolt: Res. Appl.* **2013**, DOI: 10.1002/pip.2442.

(8) Kim, J.; Hiroi, H.; Todorov, T. K.; Gunawan,O.; Kuwahara, M.; Gokmen, T.; Nair, D.; Hopstaken, M.; Shin, B.; Lee, Y. S.; Wang, W.; Sugimoto, H.; Mitzi, D. B. High Efficiency $Cu_2ZnSn(S,Se)_4$ Solar Cells by Applying a Double In_2S_3/CdS Emitter *Adv. Mater.*, DOI: 10.1002/adma.201402373.

(9) Kuo, D.-H.; Tsega, M. Electrical Conduction and Mobility Enhancement in P-type In-doped $Cu_2ZnSnSe_4$ Bulks. *Jpn. J. Appl. Phys.* **2014**, *53*, 035801.

(10) Chetty, R.; Falmbigl, M.; Rogl, P.; Heinrich, P.; Royanian, E.; Bauer, E.; Suwas, S.; Mallik, R. C. The Effect of Multisubstitution on the Thermoelectric Properties of Chalcogenide-based $Cu_{2.1}Zn_{0.9}Sn_{1-x}In_xSe_4$ ($0 \le x \le 0.1$). *Phys. Status Solidi A* **2013**, *210*, 2471.

(11) Shi, X. Y.; Huang, F. Q.; Liu, M. L.; Chen, L. D. Thermoelectric Properties of Tetrahedrally Bonded Wide-gap Stannite Compounds $Cu_2ZnSn_{1-x}In_xSe_4$. *Appl. Phys. Lett.* **2009**, *94*, 122103.

(12) Hsiao, Y.-J.; Hsueh, T.-J.; Shieh, J.; Yeh, Y.-M.; Wang, C.-C.; Dai, B.-T.; Hsu, W.-W.; Lin, J.-Y.; Shen, C.-H.; Liu, C. W.; Hu, C.; Yang, F.-L. Bifacial CIGS (11% efficiency)/Si Solar Cells by Cd-free and Sodium-free Green Process Integrated with CIGS TFTs. *2011 IEEE International Electron Devices Meeting*; IEEE: Washington, DC, 2011; pp 36.5.1–36.5.4

(13) Nakada, T.; Hirabayashi, Y.; Tokado, T.; Ohmori, D. $Cu(In_{1-x},Ga_x)Se_2$ Thin Film Solar Cells Using Transparent Conducting Oxide Back Contacts for Bifacial and Tandem Solar Cells. In *Proceedings of 3rd World Conference on Photovoltaic Energy Conversion*; IEEE: Osaka, Japan, 2003; Vol. 3, p 2880–2884.

(14) Moon, S. H.; Park, S. J.; Hwang, Y. J.; Lee, D.-K.; Cho, Y.; Kim, D.-W.; Min, B. K. Printable Wide Band-gap Chalcopyrite Thin Films for Power Generating Window Applications *Sci. Rep.* **2014**, *4*. DOI: 10.1038/srep04408.

(15) Ennaoui, A.; Lux-Steiner, M.; Weber, A.; Abou-Ras, D.; Kötschau, I.; Schock, H.-W.; Schurr, R.; Hölzing, A.; Jost, S.; Hock, R.; Voß, T.; Schulze, J.; Kirbs, A. Cu_2ZnSnS_4 Thin Film Solar Cells from Electroplated Precursors: Novel Low-cost Perspective. *Thin Solid Films* **2009**, *517*, 2511.

(16) Washio, T.; Shinji, T.; Tajima, S.; Fukano, T.; Motohiro, T.; Jimbo, K.; Katagiri, H. 6% Efficiency Cu_2ZnSnS_4-based Thin Film Solar Cells Using Oxide Precursors by Open Atmosphere Type CVD. *J. Mater. Chem.* **2012**, *22*, 4021.

(17) Schorr, S.; Tovar, M.; Hoebler, H.-J.; Schock, H.-W. Structure and Phase Relations in the $2(CuInS_2)$–Cu_2ZnSnS_4 Solid Solution System. *Thin Solid Films* **2009**, *517*, 2508–2510.

(18) Mitzi, D. B.; Gunawan, O.; Todorov, T. K.; Wang, K.; Guha, S. The Path owards a High-Performance Solution-processed Kesterite Solar Cell. *Sol. Energy Mater. Sol. Cells* **2011**, *95*, 1421.

(19) Mainz, R.; Singh, A.; Levcenko, S.; Klaus, M.; Genzel, C.; Ryan, K. M.; Unold, T. Phase-Transition-Driven Growth of Compound Semiconductor Crystals from Ordered Metastable Nanorods *Nat. Commun.* **2014**, *5*. DOI: 10.1038/ncomms4133.

(20) Fernandes, P. A.; Salomé, P. M. P.; Cunha, A. F. da Study of Polycrystalline Cu_2ZnSnS_4 Films by Raman Scattering. *J. Alloys Compd.* **2011**, *509*, 7600.

(21) Leitão, J. P.; Santos, N. M.; Fernandes, P. A.; Salomé, P. M. P.; da Cunha, A. F.; González, J. C.; Matinaga, F. M. Study of Optical and Structural Properties of Cu_2ZnSnS_4 Thin Films. *Thin Solid Films* **2011**, *519*, 7390.

(22) Shin, S. W.; Pawar, S. M.; Park, C. Y.; Yun, J. H.; Moon, J.-H.; Kim, J. H.; Lee, J. Y. Studies on Cu_2ZnSnS_4 (CZTS) Absorber Layer Using Different Stacking Orders in Precursor Thin Films. *Sol. Energy Mater. Sol. Cells* **2011**, *95*, 3202.

(23) Tani, Y.; Sato, K.; Katayama-Yoshida, H. Materials Design of $CuIn_{1-x}Zn_{0.5x}Sn_{0.5x}Se_2$ for Low Cost Photovoltaic Solar Cells. *J. Non-Cryst. Solids* **2012**, *358*, 2420.

(24) Dimitrievska, M.; Fairbrother, A.; Fontané, X.; Jawhari, T.; Izquierdo-Roca, V.; Saucedo, E.; Pérez-Rodríguez, A. Multiwavelength Excitation Raman Scattering Study of Polycrystalline Kesterite Cu_2ZnSnS_4 Thin Films. *Appl. Phys. Lett.* **2014**, *104*, 021901.

(25) Ge, J.; Jiang, J.; Yang, P.; Peng, C.; Huang, Z.; Zuo, S.; Yang, L.; Chu, A. 5.5% Efficient Co-electrodeposited ZnO/CdS/Cu_2ZnSnS_4/Mo Thin Film Solar Cell. *Sol. Energy Mater. Sol. Cells* **2014**, *125*, 20–26.

(26) Himmrich, H.; Haeuseler, H. Far Infrared Studies on Stannite and Wurtzstannite Type Compounds. *Spectrochim. Acta* **1991**, *47*, 933.

(27) Grossberg, M.; Krustok, J.; Raudoja, J.; Timmo, K.; Altosaar, M.; Raadik, T. Photoluminescence and Raman Study of $Cu_2ZnSn(Se_xS_{1-x})_4$ Monograins for Photovoltaic Applications. *Thin Solid Films* **2011**, *519*, 7403.

(28) Levcenko, S.; Tezlevan, V. E.; Arushanov, E.; Schorr, S.; Unold, T. Free-to-bound Recombination in Near Stoichiometric Cu_2ZnSnS_4 Single Crystals. *Phys. Rev. B* **2012**, *86*, 045206.

(29) Gershon, T.; Shin, B.; Bojarczuk, N.; Gokmen, T.; Lu, S.; Guha, S. Photoluminescence Characterization of a High-efficiency Cu_2ZnSnS_4 Device. *J. Appl. Phys.* **2013**, *114*, 154905.

(30) Tanaka, K.; Shinji, T.; Uchiki, H. Photoluminescence from Cu_2ZnSnS_4 Thin Films with Different Compositions Fabricated by a Sputtering-Sulfurization Method. *Sol. Energy Mater. Sol. Cells* **2014**, *126*, 143.

(31) Leitão, J. P.; Santos, N. M.; Fernandes, P. A.; Salomé, P. M. P.; da Cunha, A. F.; González, J. C.; Ribeiro, G. M.; Matinaga, F. M. Photoluminescence and Electrical Study of Fluctuating Potentials in Cu_2ZnSnS_4-based Thin Films. *Phys. Rev. B* **2011**, *84*, 024120.

(32) Yu, P. W. Excitation-dependent Emission in Mg-, Be-, Cd-, and Zn-implanted GaAs. *J. Appl. Phys.* **1977**, *48*, 5043.
(33) Schumacher, S. A.; Botha, J. R.; Alberts, V. Photoluminescence Study of Potential Fluctuations in Thin Layers of $Cu(In_{0.75}\ Ga_{0.25})(S_y\ Se_{1-y})_2$. *J. Appl. Phys.* **2006**, *99*, 063508.
(34) Dirnstorfer, I.; Wagner, M.; Hofmann, D. M.; Lampert, M. D.; Karg, F.; Meyer, B. K. Characterization of $CuIn(Ga)Se_2$ Thin Films. *Phys. Status Solidi A* **1998**, *168*, 163.
(35) Siebentritt, S.; Papathanasiou, N.; Lux-Steiner, M. C. Potential Fluctuations in Compensated Chalcopyrites. *Physica B: Condens. Matter* **2006**, *376*−*377*, 831.
(36) Levanyuk, A. P.; Osipov, V. V. Edge Luminescence of Direct-Gap Semiconductors. *Sov. Phys. Usp.* **1981**, *24*, 187.
(37) Gokmen, T.; Gunawan, O.; Todorov, T. K.; Mitzi, D. B. Band Tailing and Efficiency Limitation in Kesterite Solar Cells. *Appl. Phys. Lett.* **2013**, *103*, 103506.
(38) Shklovskii, B. I.; Efros, A. L. *Electronic Properties of Doped Semiconductors*; Springer Verlag: Berlin, 1979.
(39) Walsh, A.; Chen, S.; Wei, S.-H.; Gong, X.-G. Kesterite Thin-Film Solar Cells: Advances in Materials Modelling of Cu_2ZnSnS_4. *Adv. Energy Mater.* **2012**, *2*, 400.
(40) Han, D.; Sun, Y. Y.; Bang, J.; Zhang, Y. Y.; Sun, H.-B.; Li, X.-B.; Zhang, S. B. Deep Electron Traps and Origin of P-type Conductivity in the Earth-abundant Solar-cell Material Cu_2ZnSnS_4. *Phys. Rev. B* **2013**, *87*, 155206.
(41) Sarswat, P. K.; Free, M. L. A Study of Energy Band Gap Versus Temperature for Cu_2ZnSnS_4 Thin Films. *Physica B: Conden. Matter* **2012**, *407*, 108.
(42) Nagaoka, A.; Miyake, H.; Taniyama, T.; Kakimoto, K.; Yoshino, K. Effects of Sodium on Electrical Properties in Cu_2ZnSnS_4 Single Crystal. *Appl. Phys. Lett.* **2013**, *103*, 112107.
(43) Green, M. A.; Blakers, A. W.; Zhao, J.; Milne, A. M.; Wang, A.; Dai, X. Characterization of 23-percent Efficient Silicon Solar Cells. *IEEE Trans. Electron Devices* **1990**, *37*, 331.
(44) Glunz, S. W.; Nekarda, J.; Makel, H.; Cuevas, A. Analyzing Back Contacts of Silicon Solar Cells by Suns-V_{OC}-measurement at High Illumination Densities. In *Proceedings of the 22nd European Photovoltaic Solar Energy Conference and Exhibition*; Milan, Italy, 2007; pp 849−853.
(45) Green, M. A. Solar Cell Fill Factors: General Graph and Empirical Expressions. *Solid-State Electron.* **1981**, *24*, 788.
(46) Todorov, T. K.; Tang, J.; Bag, S.; Gunawan, O.; Gokmen, T.; Zhu, Y.; Mitzi, D. B. Beyond 11% Efficiency: Characteristics of State-of-the-Art $Cu_2ZnSn(S,Se)_4$ Solar Cells. *Adv. Energy Mater.* **2013**, *3*, 34.
(47) Demtsu, S. H.; Sites, J. R. Effect of Back-contact Barrier on Thin-film CdTe Solar Cells. *Thin Solid Films* **2006**, *510*, 320.
(48) Puttnins, S.; Levcenco, S.; Schwarzburg, K.; Benndorf, G.; Daume, F.; Rahm, A.; Braun, A.; Grundmann, M.; Unold, T. Effect of Sodium on Material and Device Quality in Low Temperature Deposited $Cu(In,Ga)Se_2$. *Sol. Energy Mater. Sol. Cells* **2013**, *119*, 281.
(49) Eisenbarth, T.; Unold, T.; Caballero, R.; Kaufmann, C. A.; Schock, H.-W. Interpretation of Admittance, Capacitance-voltage, and Current-voltage Signatures in $Cu(In,Ga)Se_2$ Thin Film Solar Cells. *J. Appl. Phys.* **2010**, *107*, 034509.
(50) Niemegeers, A.; Burgelman, M. Effects of the Au/CdTe Back Contact on IV and CV Characteristics of Au/CdTe/CdS/TCO Solar Cells. *J. Appl. Phys.* **1997**, *81*, 2881.
(51) Li, J. V.; Halverson, A. F.; Sulima, O. V.; Bansal, S.; Burst, J. M.; Barnes, T. M.; Gessert, T. A.; Levi, D. H. Theoretical Analysis of Effects of Deep Level, Back Contact, and Absorber Thickness on Capacitance−voltage Profiling of CdTe Thin-film Solar Cells. *Sol. Energy Mater. Sol. Cells* **2012**, *100*, 126.
(52) Burgelman, M.; Nollet, P.; Degrave, S. Electronic Behavior of Thin-film CdTe Solar Cells. *Appl. Phys. A: Mater. Sci. Process.* **1999**, *69*, 149.
(53) Verschraegen, J.; Burgelman, M.; Penndorf, J. Interpretation of Capacitance Measurements in $CuInS_2$-on-Cu-tape Solar Cells. *Thin Solid Films* **2004**, *451*−*452*, 179−183.
(54) Schlenker, E.; Mertens, V.; Parisi, J.; Reineke-Koch, R.; Köntges, M. Schottky Contact Analysis of Photovoltaic Chalcopyrite Thin Film Absorbers. *Phys. Lett. A* **2007**, *362*, 229.
(55) Altamura, G.; Grenet, L.; Roger, C.; Roux, F.; Reita, V.; Fillon, R.; Fournier, H.; Perraud, S.; Mariette, H. Alternative Back Contacts in Kesterite $Cu_2ZnSn(S_{1-x}Se_x)_4$ Thin Film Solar Cells. *J. Renew. Sustain. Energy* **2014**, *6*, 011401.
(56) Gunawan, O.; Todorov, T. K.; Mitzi, D. B. Loss Mechanisms in Hydrazine-processed $Cu_2ZnSn(Se,S)_4$ Solar Cells. *Appl. Phys. Lett.* **2010**, *97*, 233506.
(57) Card, H. C. Aluminum—Silicon Schottky Barriers and Ohmic Contacts in Integrated Circuits. *IEEE Trans. Electron Devices* **1976**, *ED-23*, 538.
(58) Zhou, Y.; Wang, D.; Ahyi, C.; Tin, C.-C.; Williams, J.; Park, M.; Williams, N. M.; Hanser, A.; Preble, E. A. Temperature-dependent Electrical Characteristics of Bulk GaN Schottky Rectifier. *J. Appl. Phys.* **2007**, *101*, 024506.
(59) Hackam, R.; Harrop, P. Electrical Properties of Nickel-low-doped N-type Gallium Arsenide Schottky-barrier Diodes. *IEEE Trans. Electron Devices* **1972**, *19*, 1231.
(60) Sze, S. M.; Ng, K. K. *Physics of Semiconductor Devices*, 3rd ed.; Wiley: New York, 2006.
(61) Li, J. V.; Johnston, S. W.; Li, X.; Albin, D. S.; Gessert, T. A.; Levi, D. H. Discussion of Some "Trap Signatures" Observed by Admittance Spectroscopy in CdTe Thin-film Solar Cells. *J. Appl. Phys.* **2010**, *108*, 064501.
(62) Koishiyev, G. T.; Sites, J. R.; Kulkarni, S. S.; Dhere, N. G. Determination of Back Contact Barrier Height in $Cu(In,Ga)(Se,S)_2$ and CdTe Solar Cells. In *33rd IEEE Photovoltaic Specialists Conference*; IEEE: San Diego, CA, 2008; pp 1−3.
(63) Hirsch, L.; Barrière, A. S. Electrical Characterization of InGaN/GaN Light Emitting Diodes Grown by Molecular Beam Epitaxy. *J. Appl. Phys.* **2003**, *94*, 5014.
(64) Xin, H.; Katahara, J. K.; Braly, I. L.; Hillhouse, H. W. 8% Efficient $Cu_2ZnSn(S,Se)_4$ Solar Cells from Redox Equilibrated Simple Precursors in DMSO. *Adv. Energy Mater.* **2014**, *4*, 1301823.
(65) Carter, N. J.; Yang, W.-C.; Miskin, C. K.; Hages, C. J.; Stach, E. A.; Agrawal, R. $Cu_2ZnSn(S,Se)_4$ Solar Cells from Inks of Heterogeneous Cu−Zn−Sn−S Nanocrystals. *Sol. Energy Mater. Sol. Cells* **2014**, *123*, 189.
(66) Schnabel, T.; Löw, M.; Ahlswede, E. Vacuum-free Preparation of 7.5% Efficient $Cu_2ZnSn(S,Se)_4$ Solar Cells Based on Metal Salt Precursors. *Sol. Energy Mater. Sol. Cells* **2013**, *117*, 324.
(67) Gunawan, O.; Gokmen, T.; Warren, C. W.; Cohen, J. D.; Todorov, T. K.; Barkhouse, D. A. R.; Bag, S.; Tang, J.; Shin, B.; Mitzi, D. B. Electronic Properties of the $Cu_2ZnSn(Se,S)_4$ Absorber Layer in Solar Cells as Revealed by Admittance Spectroscopy and Related Methods. *Appl. Phys. Lett.* **2012**, *100*, 253905.

NOTE ADDED AFTER ASAP PUBLICATION

This paper was published on the Web on November 6, 2014, with minor text errors. The corrected version was reposted on November 7, 2014.